Available online at www.sciencedirect.com

ScienceDirect

Geochimica et Cosmochimica Acta 296 (2021) 1–17

Geochimica et Cosmochimica Acta

www.elsevier.com/locate/gca

Diverse serpentinization and associated abiotic methanogenesis within multiple types of olivine-hosted fluid inclusions in orogenic peridotite from northern Tibet

Long Zhang [a,*], Qiang Wang [a,b,c], Xing Ding [a], Wan-Cai Li [d,e]

[a] State Key Laboratory of Isotope Geochemistry, Guangzhou Institute of Geochemistry, Chinese Academy of Sciences, Guangzhou 510640, China
[b] CAS Center for Excellence in Tibetan Plateau Earth Sciences, Beijing 100101, China
[c] College of Earth and Planetary Sciences, University of Chinese Academy of Sciences, Beijing 100049, China
[d] CAS Key Laboratory of Crust-Mantle Materials and Environments, School of Earth and Space Sciences, University of Science and Technology of China, Hefei 230026, China
[e] CAS Center for Excellence in Comparative Planetology, University of Science and Technology of China, Hefei 230026, China

Received 20 August 2020; accepted in revised form 21 December 2020; available online 30 December 2020

Abstract

Hydrothermal fluids percolating through peridotite are highly enriched in abiotic CH_4, which can fuel chemosynthetic microbial activity and potentially early life. In contrast to the paradigm favoring coupled abiotic methanogenesis and fluid circulation, recent studies have suggested that leaching of CH_4 included in peridotite can account for elevated levels of CH_4 in serpentinization fluids. As such, CH_4 venting at continental gas seepage hosted in orogenic peridotite should be derived mostly from CH_4 that originated within the host peridotite. However, the origin of CH_4 included in orogenic peridotite remains elusive, as the included CH_4 is reported to form either in situ during serpentinization within fluid inclusions, or to originate from reduced external fluids. Moreover, varying associations of step-daughter minerals documented in CH_4-bearing fluid inclusions in orogenic peridotite demonstrate the diversity of fluid–mineral interactions within fluid inclusions. Here we present a detailed petrological investigation into olivine-hosted CH_4-bearing fluid inclusions in ophiolitic harzburgite from the North Qilian orogen in northern Tibet, which reveals the occurrence of abiotic CH_4 synthesis during diverse serpentinization within multiple types of olivine-hosted fluid inclusions. Three types of CH_4-bearing fluid inclusions are newly identified in the harzburgite. Type I fluid inclusions contain $CH_{4(g)}$ + antigorite + brucite + magnetite + magnesite, which imply abiotic CH_4 synthesis during hydration of olivine directly into antigorite. This contradicts the previous proposal that suggests the inhibition of H_2 and CH_4 production during high-temperature serpentinization in the stability field of antigorite. Type II fluid inclusions consist of $CH_{4(g)} + N_{2(g)}$ + lizardite + brucite ± magnetite or $CH_{4(g)} + N_{2(g)}$ + lizardite + magnetite, with brucite-bearing inclusions yielding less CH_4 compared with brucite-free inclusions. The crystallization of brucite in type II fluid inclusions was probably controlled by the concentration of dissolved Si in the trapped fluids. Type III fluid inclusions are composed of $CH_{4(g)}$ + antigorite + magnesite + graphite ± magnetite ± dolomite. High concentrations of oxidized inorganic carbon in type III fluid inclusions likely promoted the precipitation of carbonate and crystallization of antigorite. Moreover, the presence of relict lizardite in minor type III fluid inclusions suggests that antigorite growth accompanying carbonate saturation is probably a two-step process, with initial hydration of olivine into lizardite being followed by transformation of lizardite into antigorite. Above all, this study demonstrates that CH_4-bearing fluid inclusions in orogenic peridotite can be very abundant, and may be a significant reservoir of abiotic CH_4 in serpentinite-hosted hydrothermal systems. Moreover, the multiple types of CH_4-bearing fluid inclusions in orogenic peridotite presented in this study indicate that olivine-hosted

* Corresponding author.
E-mail address: zhanglong@gig.ac.cn (L. Zhang).

https://doi.org/10.1016/j.gca.2020.12.016

CH_4-bearing fluid inclusions can potentially be a novel window for studying abiotic CH_4 synthesis during serpentinization under different conditions.

Keywords: Serpentinization; CH_4; Fluid inclusions; Olivine; Orogenic peridotite; North Qilian

1. INTRODUCTION

Deep-sea and on-land serpentinite-hosted hydrothermal fluids are highly enriched in H_2 and CH_4, which have been a focus of great interest for the scientific community owing to their role in supporting chemosynthetic microbes and potentially early life (McCollom and Seewald, 2013; Schrenk et al., 2013; Ménez, 2020). It is well established that large quantities of H_2 are produced by reduction of H_2O during serpentinization via oxidation of ferrous Fe, mainly in olivine and pyroxenes (Evans et al., 2013; McCollom and Seewald, 2013; Klein et al., 2020). Theoretical and experimental efforts have constrained the reaction pathways of H_2 production during serpentinization (Klein et al., 2009, 2013; McCollom and Bach, 2009; McCollom et al., 2016), although it remains to be further clarified whether sufficient H_2 can be produced at low temperatures in the realm of microbial activity (Klein et al., 2020) or at high temperatures in the stability field of antigorite (Evans, 2010). Regarding CH_4, the current paradigm favors its abiotic formation by Fischer-Tropsch-type (FTT; including the Fischer-Tropsch and Sabatier reactions, etc.) synthesis from inorganic carbon ($\Sigma CO_2 = CO_{2(aq)} + H_2CO_3 + HCO_3^- + CO_3^{2-}$) and H_2 (Etiope and Schoell, 2014; Etiope and Whiticar, 2019). However, mass balance and isotopic constraints have revealed that abiotic CH_4 synthesis is probably decoupled from active fluid circulation in ultramafic rocks (McDermott et al., 2015; Wang et al., 2018). Moreover, experimental simulations have demonstrated that abiotic CH_4 synthesis during serpentinization is kinetically inhibited unless efficiently catalyzed (McCollom, 2013, 2016). Therefore, the origin of abiotic CH_4 in serpentinite-hosted hydrothermal vents remains inconclusive.

Recent studies have suggested that leaching of CH_4-bearing fluid inclusions in olivine-rich rocks can contribute to the CH_4 inventory in both submarine and subaerial hydrothermal systems (McDermott et al., 2015; Klein et al., 2019; Grozeva et al., 2020). It has been discovered that CH_4 synthesis associated with internal serpentinization within olivine-hosted fluid inclusions is widespread in abyssal and orogenic peridotites (Klein et al., 2019; Grozeva et al., 2020). In this respect, CH_4 included in peridotite may be a major source of CH_4 venting at continental gas seepage hosted in orogenic peridotite. Previous studies have also reported the presence of CH_4-rich fluid inclusions within olivine in orogenic peridotite (Liu and Fei, 2006; Sachan et al., 2007; Song et al., 2009; Katayama et al., 2010; Miura et al., 2011; Arai et al., 2012). However, the included CH_4 was interpreted to be sourced mostly from external reduced fluids (Liu and Fei, 2006; Sachan et al., 2007; Song et al., 2009; Katayama et al., 2010; Arai et al., 2012). Therefore, the origin of CH_4 included in orogenic peridotite remains unclear as it can be synthesized in situ or derived ex situ. Even for CH_4 synthesized during in situ serpentinization within fluid inclusions in orogenic peridotite, varying internal fluid–mineral interactions are revealed by diverse step-daughter minerals that form within fluid inclusions owing to the interaction of trapped fluids with host minerals (Miura et al., 2011; Klein et al., 2019; Grozeva et al., 2020).

In this study, we present a detailed petrological investigation into multiple types of olivine-hosted CH_4-bearing fluid inclusions newly identified in the Yushigou ophiolitic harzburgite from the North Qilian orogen in northern Tibet. The Yushigou harzburgite has been reported to contain olivine-hosted primary CH_4-rich fluid inclusions entrapped from external reduced fluids during the growth of olivine (Song et al., 2009). In contrast, we provide evidence that CH_4 in fluid inclusions in the Yushigou harzburgite was synthesized during internal serpentinization within fluid inclusions. Moreover, we demonstrate that different types of CH_4-bearing fluid inclusions, which equilibrated under different conditions, are present in the Yushigou harzburgite. Above all, unusually abundant and diverse CH_4-bearing fluid inclusions in the Yushigou harzburgite indicate that CH_4-bearing fluid inclusions in orogenic peridotite may not only be a significant reservoir of abiotic CH_4, but also constitute a new approach for studying serpentinization and associated abiotic CH_4 synthesis.

2. GEOLOGICAL SETTING AND SAMPLES

The North Qilian orogen is a typical oceanic suture zone in the northeastern margin of the Great Tibetan plateau (Fig. S1). It comprises early Paleozoic ophiolite sequences, high pressure metamorphic rocks, and island-arc magmatic rocks, as well as Silurian flysches, Devonian molasses, and Carboniferous to Triassic sediments (Song et al., 2013). Ophiolite suites in the North Qilian orogen are spatially divided into the southern and northern belts. The Yushigou ophiolite, located in the west of the southern ophiolite belt, hosts the largest ultramafic body in the North Qilian orogen (Fig. S1). Fault-bounded ultramafic rocks in the Yushigou ophiolite are mostly severely serpentinized and carbonated. However, minor fresh peridotite blocks dominated by harzburgite with subordinate dunite and pyroxenite crop out along mountain ridges.

Fresh Yushigou harzburgite is composed mainly of olivine and orthopyroxene with subordinate spinel and clinopyroxene (Fig. S2). The harzburgite has undergone only negligible alteration along fractures and mineral boundaries. Loss on ignition (LOI) of the fresh harzburgite is generally less than 1–2%, with some samples displaying

negative LOI. The low LOI also shows that secondary alteration is limited in the peridotite, consistent with petrographic observation. The petrology and geochemistry of the Yushigou harzburgite indicate that the harzburgite is typical of forearc mantle residual peridotite (Song et al., 2009, 2013; Zhang et al., 2019a), and the Yushigou ophiolite is a supra-subduction zone (SSZ) ophiolite. The harzburgite has been subjected to plastic deformation under near-solidus conditions, developing crystal preferred orientations of olivine and orthopyroxene and slight foliation in the matrix (Cao et al., 2015). Methane-dominated fluid inclusions with lesser other gases or graphite have been reported in olivine from a Yushigou harzburgite by Song et al. (2009). As these fluid inclusions, which apparently lacked serpentine and magnetite, partly resemble primary fluid inclusions in distribution and morphology, it has been proposed that CH_4 included in the Yushigou harzburgite is a primary fluid species entrapped during the growth of olivine (Song et al., 2009). Moreover, these CH_4-rich fluid inclusions have been taken as evidence for metasomatism of the mantle wedge by reduced fluids derived from the subducting slab (Song et al., 2009).

3. ANALYTICAL METHOD

Double-polished thin sections of fresh Yushigou harzburgite samples were firstly examined for fluid inclusions using an optical microscope. Raman spectra of representative fluid inclusions were then obtained using a WITec alpha 300R confocal Raman spectrometer (at the State Key Laboratory of Isotope Geochemistry, Guangzhou Institute of Geochemistry, Guangzhou, China) equipped with three lasers (488, 532, and 633 nm), three gratings (300, 600, and 1800 grooves/mm), and a back-illuminated charge-coupled detector (1600 × 200 pixels). The Raman spectrometer was calibrated regularly using Ar and Ne lamps, and twice a day using a standard silicon wafer during daily analysis period. Routine spot Raman spectra of fluid inclusions were acquired using the 488 nm laser, the 300 mm^{-1} grating, and a 100 × Zeiss objective (numerical aperture = 0.9). To calculate the CH_4 vapor pressure in fluid inclusions (Lu et al., 2007), the Raman shift of the C—H symmetric stretching band (υ1) of $CH_{4(g)}$ was measured using the 632 nm laser, the 1800 mm^{-1} grating, and the 100 × Zeiss objective. Single-spot Raman spectra were refined by averaging 5–10 acquisition sequences, with acquisition times of 5–30 s per sequence. Besides spot analyses, hyperspectral Raman mapping of representative fluid inclusions was accomplished using the 488 nm laser, the 300 mm^{-1} grating, and the 100 × Zeiss objective, with acquisition times of 15–30 s and x–y step sizes of 0.5–1.0 μm. Raman spectra were processed with the Control Five software that came with the Raman spectrometer. Identification of Raman peaks was based on reference phase spectra from the literature (Rinaudo et al., 2003; Frezzotti et al., 2012). However, Raman peaks of graphite deviated from standard positions owing to intrinsic structural heterogeneity, varying crystallographic orientation, and the high laser power used to analyze fluid inclusions (Beyssac and Lazzeri, 2012).

Opened CH_4-bearing fluid inclusions were examined by scanning electron microscope and electron probe microanalyzer (EPMA). Olivine grains separated from crushed samples were embedded in epoxy resin and carefully polished to expose an internal surface. Opened fluid inclusions were firstly located using reflected light under an optical microscope and then analyzed by Raman spectrometer. Back-scattered electron (BSE) images and semi-quantitative analyses of opened fluid inclusions were obtained using a SUPRA 55 SAPPHIRE field-emission scanning electron microscope equipped with an Oxford Inca250 X-Max20 energy dispersive spectrometer (at the State Key Laboratory of Isotope Geochemistry, Guangzhou Institute of Geochemistry). The accelerating voltage and the beam current were set at 15 kV and 10 nA, respectively. Element distribution maps and quantitative analyses of opened fluid inclusions were acquired using a JEOL JXA 8530F field-emission EPMA (at the CAS Key Laboratory of Crust-Mantle Materials and Environments, University of Science and Technology of China, Hefei, China). Element mapping of opened fluid inclusions was accomplished with an accelerating voltage of 15 kV, a beam current of 200 nA, a x–y step size of 0.1–0.2 μm, and an acquisition time of 200 ms at each point. Major-element analyses of host olivine and step-daughter minerals in opened fluid inclusions were carried out with an accelerating voltage of 15 kV, a beam current of 10 nA, and a beam radius of 3 μm. Natural and synthetic standards were used for element calibration, and the ZAF method was used for data correction. Step-daughter minerals in opened fluid inclusions were distinguished and identified based on a combination of Raman spectra, BSE images, semi-quantitative analyses, and quantitative analyses.

4. PETROLOGRAPHY AND COMPOSITION OF CH_4-BEARING FLUID INCLUSIONS

Abundant and diverse CH_4-bearing polyphase fluid inclusions, composed of solid and gaseous phases, are observed in olivine from the Yushigou harzburgite (Figs. 1 and 2). The vast majority of olivine grains separated from crushed samples contains varying amounts of CH_4-bearing polyphase fluid inclusions. The inclusions are interpreted to have originally contained only fluid phase, with the solid and gaseous phases that are now present being the result of post-trapping fluid–host interactions. No free H_2O was detected in any fluid inclusion by Raman spectroscopy, indicating possible complete consumption during internal fluid–host interactions. These CH_4-bearing fluid inclusions can be categorized into three types according to their distribution, morphology, and composition. The main characteristics of the three types of CH_4-bearing fluid inclusions are listed in Table 1.

Type I fluid inclusions are scarce, occurring mostly as prismatic inclusions in oriented clusters in the interior of olivine grains (Fig. 1a and b). Moreover, these fluid inclusions are parallel to the foliation of the harzburgite, which is indicated by preferred orientation of olivine and orthopyroxene with large grain sizes and high aspect ratios. The long axes of type I fluid inclusions vary from several

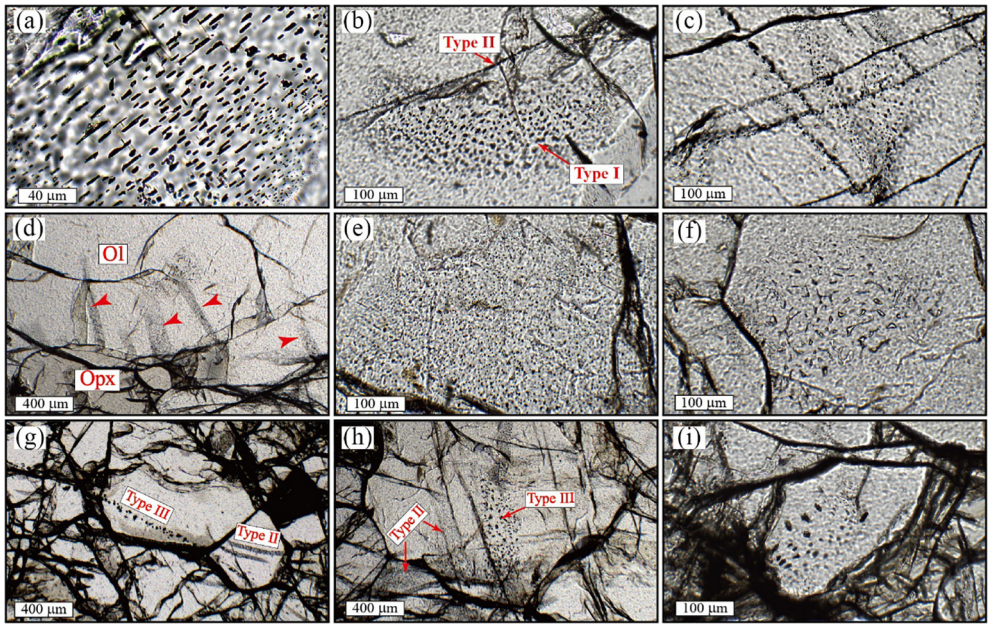

Fig. 1. Photomicrographs showing distributions of multiple types of CH_4-bearing fluid inclusions in olivine from the Yushigou harzburgite. (a) Oriented and elongated type I fluid inclusions with decreasing sizes toward olivine rim. (b) A cluster of type I fluid inclusions in the interior of olivine crosscut by a trail of type II fluid inclusions. (c) Crosscutting trails of type II fluid inclusions. (d) Planes of type II fluid inclusions (indicated by the red arrows) extending from the grain boundary into the interior of olivine. (e) Densely distributed type II fluid inclusions in an olivine grain. (f) A cluster of vermicular type II fluid inclusions extending from grain boundary into the interior of olivine. (g) A trail of transgranular coarse-grained type III fluid inclusions compared with trails of fine-grained type II fluid inclusions. (h) Planes of coarse-grained type III fluid inclusions compared with planes and patches of fine-grained type II fluid inclusions. (i) A patch of type III fluid inclusions with varying sizes. Mineral abbreviations in this study are after Whitney and Evans (2010).

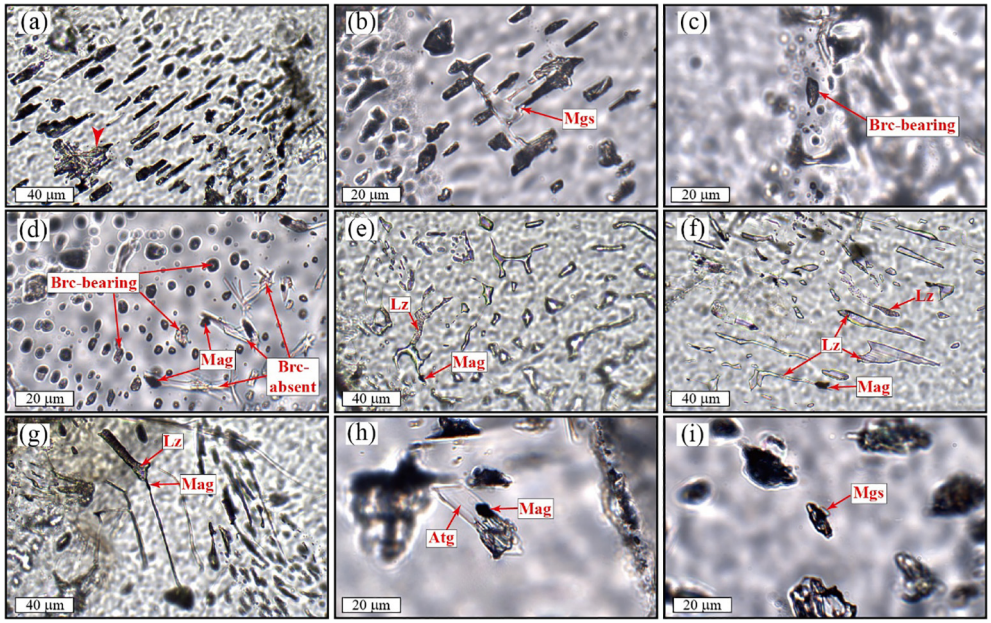

Fig. 2. Close-up views of representative CH_4-bearing fluid inclusions in olivine from the Yushigou harzburgite. (a) Mostly prismatic type I fluid inclusions with a few decrepitated examples (indicated by the red arrow). (b) Type I fluid inclusions with necking-down texture. (c) Spindle-shaped type II fluid inclusion composed of $CH_{4(g)} + N_{2(g)}$ + lizardite + brucite. (d) Coexisting brucite-bearing and brucite-absent type II fluid inclusions. Brucite-bearing type II fluid inclusions show weak orientation. (e) Vermicular type II fluid inclusions with recognizable magnetite and lizardite. (f) Cuspate type II fluid inclusions with magnetite and lizardite present. (g) Type II fluid inclusion with necking-down texture. Transparent parts of fluid inclusions in (e)–(g) are a mixture of $CH_{4(g)}$ and $N_{2(g)}$. (h) A type III fluid inclusion with well-crystallized antigorite and magnetite. (i) A type III fluid inclusion with an isolated magnesite grain.

Table 1
Summary of the main characteristics of the three types of olivine-hosted fluid inclusions identified in the Yushigou harzburgite.

No.	Category	Type	Abundance[1]	Distribution	Size (μm)	Morphology	Detected phases[2]	$CH_{4(g)}$ Raman (cm^{-1})	Serpentinization reaction
I	/	Primary	-	Oriented clusters in the interior of Ol	5–80	Prismatic to irregular	CH_4 (++), Atg (++), Brc (++), Mag (++), Mgs (++), Gr (+), Pn (−)	2913–2915	$34Fo + 51H_2O = Atg + 20Brc$
II	Brc-bearing	Secondary	++	Intragranular trails, planes, and patches	1–20	Ellipsoid to irregular	CH_4 (++), N_2 (++), Lz (++), Brc (++), Mag (+), Gr (−), H_2 (−)	2914–2916	$2Fo + 3H_2O = Lz + Brc$
	Brc-free				1–120	Irregular	CH_4 (++), N_2 (++), Lz (++), Brc (−), Mag (++), Gr (+), H_2 (−)	2911–2914	$2Fo + 3H_2O = Lz + Brc$ $3Brc + 2SiO_2{}_{(aq)} = Lz + H_2O$
III	/	Secondary	+	Intragranular to transgranular trails, planes, and patches	5–40	Irregular	CH_4 (++), Atg (++), Gr (++), Mag (++), Mgs (++), Dol (+), Lz (−), H_2 (−), Pn (−)	2913–2914	$2Fo + 3H_2O = Lz + Brc$ $16Lz + 2SiO_2{}_{(aq)} = Atg + H_2O$

[1] ++ vey abundant, + abundant, - scarce
[2] ++ very common, + common, - scarce.

micrometers to about 80 μm, whereas the short axes vary from several micrometers to about 20 μm. Some type I fluid inclusions display irregular shapes owing to decrepitation and uncompleted necking-down with splitting of a large inclusion into several smaller inclusions (Fig. 2a and b). Type I fluid inclusions are composed mainly of $CH_{4(g)}$, antigorite, brucite, magnesite, and magnetite (Fig. 3a–d, 4, 5, and S3). Graphite and pentlandite (Fig. 5) are observed in some type I fluid inclusions. Methane in type I fluid inclusions has a Raman υ1 band ranging from 2913 to 2915 cm^{-1} (Fig. 6a; Table S1), corresponding to a partial pressure range of 15.2–28.4 MPa.

Type II fluid inclusions are the most abundant and are present in every sample. They occur in intragranular trails (Fig. 1c), planes (Fig. 1d), and patches (Fig. 1e and f), extending from the grain boundary to the interior of olivine grain or to another grain boundary (Fig. 1d and f). Several generations of type II fluid inclusions are present, as illustrated by their crosscutting relationships (Fig. 1c). Trails of type II fluid inclusions crosscutting type I fluid inclusions can be observed (Fig. 1b). Most type II fluid inclusions are randomly distributed, though a few clusters show a weak preferred orientation (Figs. 1e and 2d). Type II fluid inclusions range from several micrometers to more than 100 μm in size. They vary greatly in morphology, displaying either regular or irregular shapes (Fig. 2c–g). Type II fluid inclusions consist of either $CH_{4(g)} + N_{2(g)}$ + lizardite + brucite ± magnetite ± graphite or $CH_{4(g)} + N_{2(g)}$ + lizardite + magnetite ± graphite (Figs. 3e–f, 7, and 8). Hydrogen was identified in a few type II fluid inclusions (Fig. 3e). In contrast to types I and III fluid inclusions, carbonate was rarely detected in type II fluid inclusions. Brucite-bearing type II fluid inclusions are generally semitransparent with regular morphologies, such as sphere and spheroid (Fig. 2c–d and 7a). They are mostly smaller than 5–10 μm, with a few reaching 10–20 μm (Fig. 2c–d, 7a, and 8a). In contrast, brucite-absent type II fluid inclusions are mostly transparent, with magnetite and lizardite optically observable in some large inclusions (Fig. 2d–g and 7b). They vary greatly in size from smaller than 5–10 μm to larger than 100 μm (Fig. 2d–g, 7b, and 8b). Brucite-absent type II fluid inclusions larger than 20 μm are quite common and generally have irregular morphologies with cuspate endings and stretching tentacles (Fig. 2d–g and 7b). The Raman υ1 band of $CH_{4(g)}$ in brucite-bearing type II fluid inclusions ranges from 2914 to 2916 cm^{-1} (Fig. 6b; Table S1), with a calculated vapor pressure range of 10.4–20.6 MPa. In contrast, the Raman υ1 band of $CH_{4(g)}$ in brucite-absent type II fluid inclusions varies from 2911 to 2914 cm^{-1} (Fig. 6b; Table S1), corresponding to higher partial pressures of 20.6–76.9 MPa. However, the calculated partial pressure of $CH_{4(g)}$ in type II fluid inclusions is likely to be an underestimate, as the presence of $N_{2(g)}$ can reduce the Raman shift of the $CH_{4(g)}$ υ1 band (Fabre and Oksengorn, 1992; Seitz et al., 1993). Type II fluid inclusions in some clusters are too tiny to determine whether brucite is present, but they generally have $CH_{4(g)}$ υ1 bands similar to those of brucite-bearing fluid inclusions.

Type III fluid inclusions are also abundant, but much less so than type II fluid inclusions. They occur in

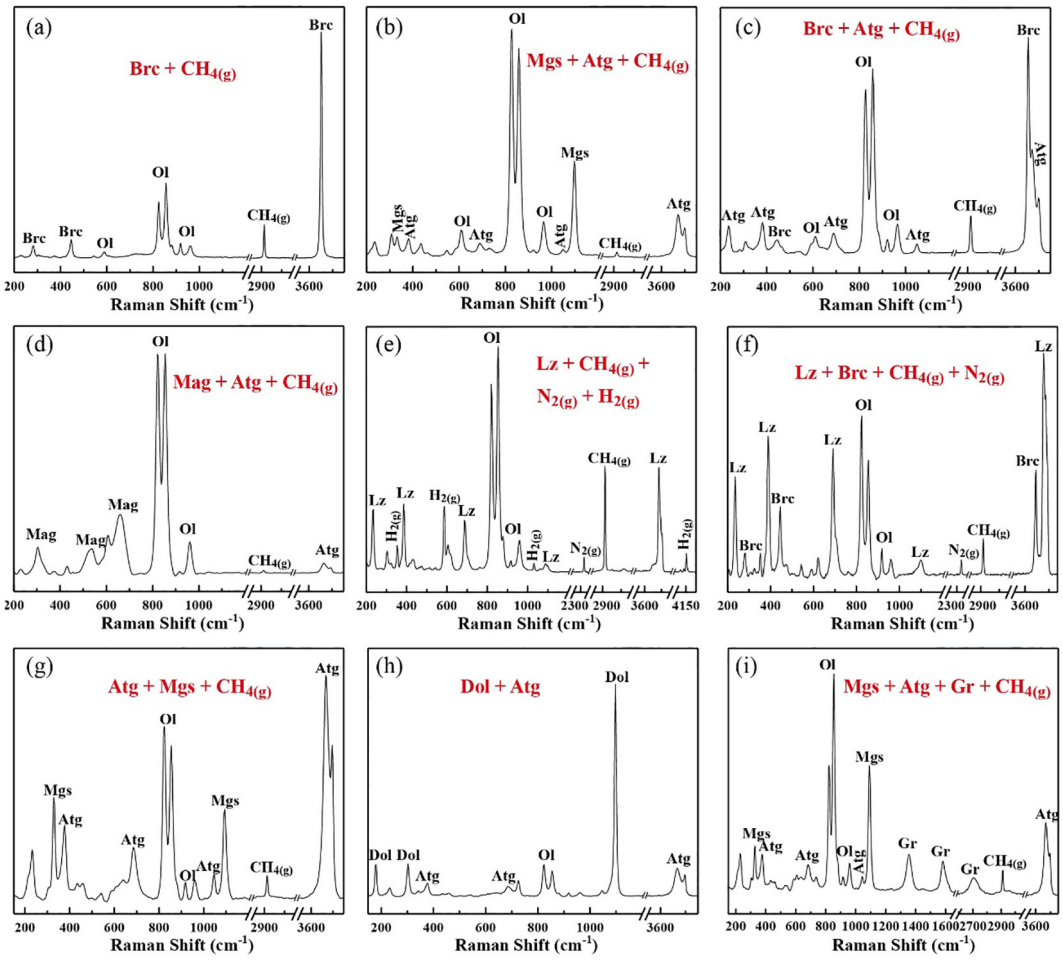

Fig. 3. Representative single spot Raman spectra of CH_4-bearing fluid inclusions in olivine from the Yushigou harzburgite. (a)–(d) Type I fluid inclusions. (e)–(f) Type II fluid inclusions. (g)–(i) Type III fluid inclusions.

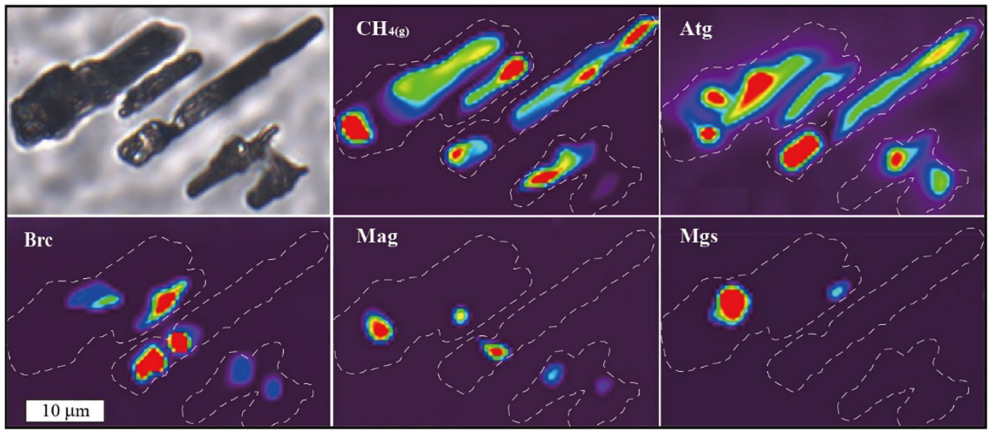

Fig. 4. Hyperspectral Raman mapping of a typical type I CH_4-bearing fluid inclusion compared with the photomicrograph of the mapped fluid inclusion. Warmer color in Raman mapping in all figures represents higher Raman signal intensity for the marked phase.

intragranular to transgranular trails (Fig. 1g), planes (Fig. 1h), and patches (Fig. 1i). Type III fluid inclusions locally crosscut or grade into brucite-bearing type II fluid inclusions (Fig. 1h). Moreover, type III fluid inclusions are larger on average than neighboring type II fluid inclusions (Fig. 1g and h), with the sizes of most type III fluid inclusions reaching 5–40 μm (Fig. 2h–i, 9, 10, and S4). Type III fluid inclusions are composed of $CH_{4(g)}$ + antigorite

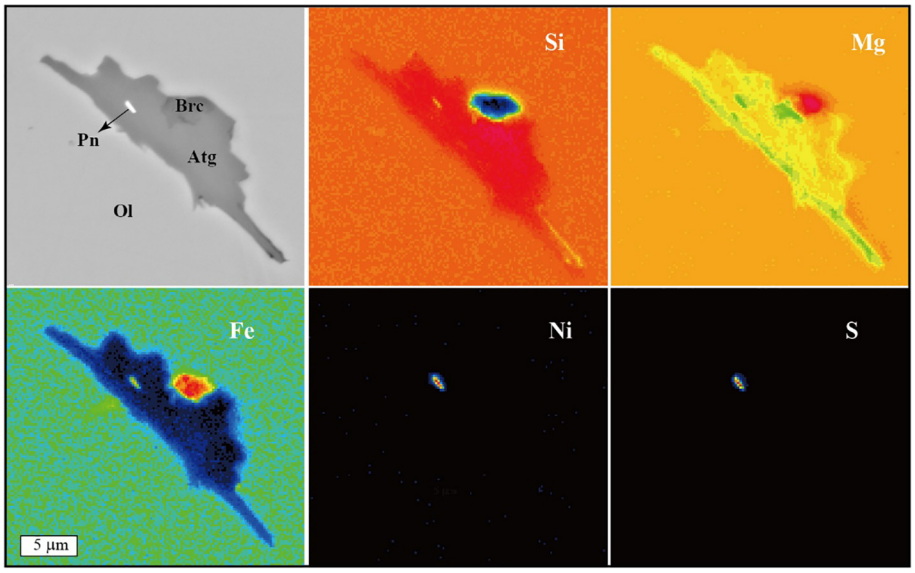

Fig. 5. BSE image and element mapping of an opened type I CH_4-bearing fluid inclusion. Warmer color in element distribution maps in all figures represents higher concentration for the marked element.

+ magnesite + graphite ± magnetite ± dolomite ± pentlandite ± lizardite (Fig. 3g–i, 9, 10, and S4). It is noted that antigorite in most cases occurs with carbonate minerals in type III fluid inclusions. Magnetite, magnesite, and well-crystallized antigorite blades could be optically observed in some type III fluid inclusions (Fig. 2h–i). Nitrogen could not be detected in most type III FIs. Hydrogen was identified in several type III fluid inclusions. Moreover, lizardite was locally detected to coexist with antigorite in a few type III fluid inclusions (Fig. S5). Except for one sample, $CH_{4(g)}$ in type III fluid inclusions mostly has a Raman υ1 band of 2913–2914 cm^{-1} (Fig. 6c; Table S1), corresponding to a partial pressure range of 20.6–28.4 MPa.

The analytical results for major-element compositions of host olivine and step-daughter minerals in opened CH_4-bearing fluid inclusions are listed in Table S2. The olivine hosts of the CH_4-bearing fluid inclusions are relatively homogeneous, with Mg# (=Mg/(Mg + Fe) in moles) of 0.91–0.92. Antigorite in type III fluid inclusions is also uniform in composition, with higher Mg# of 0.96–0.97 and high Si atoms per formula unit (apfu; normalized to 7 oxygen ions) of 2.04–2.08 (Fig. 11). Opened type I fluid inclusions are rare, with one antigorite blade (Table S2, No. 1) showing a similar composition to that of antigorite in type III fluid inclusions. Another antigorite blade (Table S2, No. 2) intergrown with brucite contains lower Si apfu and higher Mg + Fe apfu (Fig. 11). Analysis of brucite and antigorite mixtures (Table S2, No. 3) indicates the significant presence of Fe in brucite, which is also supported by element mapping (Fig. 5). Lizardite in type II fluid inclusions shows varying extents of intergrowth with brucite, which is characterized by Mg# of 0.89–0.99 and Si apfu of 1.81–2.01 (Fig. 11). Brucite in type II fluid inclusions is generally too small to allow accurate analysis. Carbonate in type III fluid inclusions is mostly magnesite with subordinate dolomite (Fig. 12). Magnesite in type III fluid inclusions contains considerable FeO (2.44–8.29%) and minor CaO (0.04–1.29%). In contrast, dolomite in type III fluid inclusions contains less FeO (1.00–1.40%).

5. DISCUSSION

5.1. In situ formation of $CH_{4(g)}$ in fluid inclusions within olivine in orogenic peridotite

Methane included within olivine-hosted fluid inclusions in orogenic peridotite may originate from the following: (1) entrapment of CH_4-bearing reduced fluids from external sources (Liu and Fei, 2006; Sachan et al., 2007; Song et al., 2009; Katayama et al., 2010; Arai et al., 2012); (2) re-speciation of initial CO_2–H_2O fluids with attendant graphite precipitation during cooling (Kelley, 1996; Kelley and Früh-Green, 1999, 2001); (3) in situ CH_4 synthesis via reduction of ΣCO_2 by external $H_{2(g)}$, for example, generated during matrix serpentinization, diffused into fluid inclusions (Hall and Bodnar, 1990; Hall et al., 1991; Mavrogenes and Bodnar, 1994); or (4) in situ CH_4 synthesis via reduction of ΣCO_2 by $H_{2(g)}$ generated during internal serpentinization during cooling (Miura et al., 2011; Klein et al., 2019; Grozeva et al., 2020). The assemblage of serpentine, magnetite, brucite, $H_{2(g)}$, and carbonates in CH_4-bearing fluid inclusions from the Yushigou harzburgite demonstrates that fluid–olivine interaction in fluid inclusions have certainly taken place, favoring the in situ formation of $CH_{4(g)}$ via reduction of ΣCO_2 by $H_{2(g)}$ produced during internal serpentinization.

However, there is a need to determine whether other mechanisms could have contributed to the $CH_{4(g)}$ budget in fluid inclusions from the Yushigou harzburgite. Infiltration by primary external CH_4-bearing reduced fluids into the Yushigou harzburgite, as suggested by a previous study (Song et al., 2009), is unlikely, as the harzburgite has a high

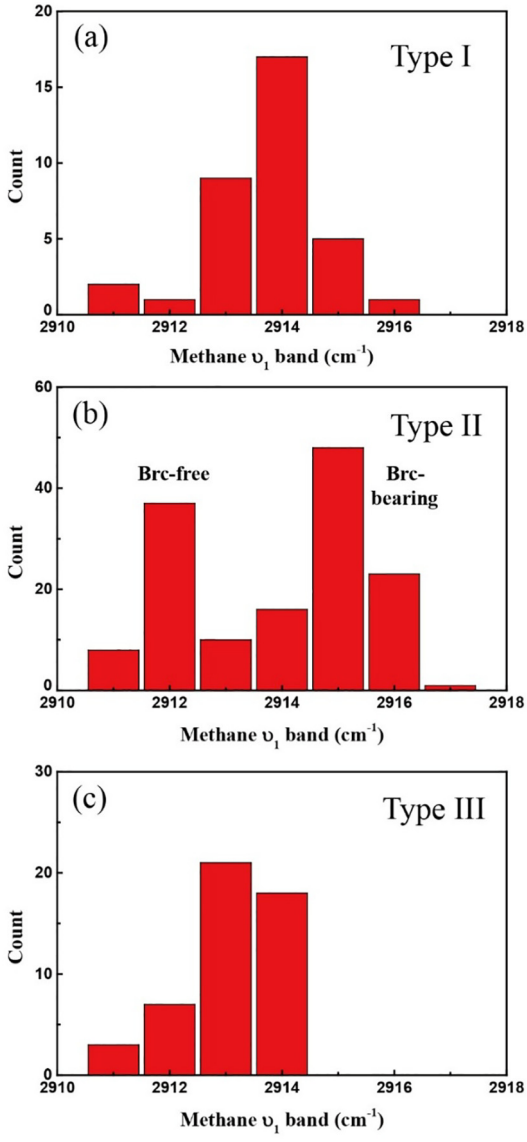

Fig. 6. Raman shift of the C–H symmetric stretching band (υ1) of $CH_{4(g)}$ included in (a) type I, (b) type II, and (c) type III fluid inclusions.

oxygen fugacity of FMQ + 0.57–1.02 (Zhang et al., 2019a). Moreover, carbonate minerals in fluid inclusions from the harzburgite indicate that the initial trapped fluids were probably oxidized. Re-speciation of CO_2–H_2O fluid inclusions with attendant graphite precipitation generally produces CO_2–CH_4–H_2O fluids that are in disequilibrium with host olivine (Kelley, 1996; Kelley and Früh-Green, 1999, 2001). Furthermore, graphite is not ubiquitous in all olivine-hosted fluid inclusions from the Yushigou harzburgite. Diffusion of external $H_{2(g)}$ into fluid inclusions was unlikely during internal serpentinization in fluid inclusions, as serpentinization of olivine in fluid inclusions is generally more reducing compared with serpentinization of olivine–orthopyroxene matrix (Klein et al., 2013). Moreover, the peridotite is rather fresh, with limited serpentinization and $H_{2(g)}$ generation. After the completion of fluid–olivine interaction in fluid inclusions, external $H_{2(g)}$ might diffuse into fluid inclusions owing to a reversed fH_2 gradient. However, fluids should have been consumed in fluid inclusions with the transformation of ΣCO_2 into $CH_{4(g)}$ or carbonates, which could hardly be further reduced by $H_{2(g)}$. Therefore, $CH_{4(g)}$ in the fluid inclusions was most likely derived from the reduction of ΣCO_2 by $H_{2(g)}$ produced during internal serpentinization, with insignificant contributions from other mechanisms.

Serpentine and brucite could be produced in the fluid inclusions by the reaction of H_2O with the contacting olivine wall during cooling of the harzburgite, according to the following generalized reaction that can operate at 50–600 °C (Evans, 2010):

$$\text{olivine} + H_2O \rightarrow \text{serpentine} + \text{brucite}. \quad (1)$$

Hydrogen generation by the reduction of H_2O is coupled to the oxidation of ferrous Fe in olivine into ferric Fe in serpentine and magnetite via the simplified reaction:

$$2FeO + H_2O = Fe_2O_3 + H_2. \quad (2)$$

The hydrogen produced can reduce ΣCO_2 into CH_4 via the FTT reaction:

$$CO_2 + 4H_2 = CH_4 + 2H_2O. \quad (3)$$

Exhaustion as a reactant during the FTT reaction or loss via diffusion may explain the lack of $H_{2(g)}$ in most fluid inclusions. Preservation of $H_{2(g)}$ in some fluid inclusions may be attributable to the generation of some external $H_{2(g)}$ during matrix serpentinization, which could decrease the fH_2 gradient between the fluid inclusions and matrix fluids. Carbonates were precipitated in types I and III fluid inclusions owing to saturation of ΣCO_2. In contrast, ΣCO_2 was probably exhausted during the FTT reaction in type II fluid inclusions, without the precipitation of carbonates. Poorly crystallized graphite (Figs. 3i and 9) is common in types III and I fluid inclusions, but it is unclear whether the graphite was precipitated owing to post-entrapment re-equilibration of ΣCO_2 during cooling (Kelley, 1996; Kelley and Früh-Green, 1999, 2001) or ΣCO_2 reduction by H_2 generated during serpentinization (Andreani and Ménez, 2019).

Most previous studies reporting CH_4-bearing fluid inclusions within olivine in orogenic peridotite (including the Yushigou harzburgite) have suggested an external source for the included $CH_{4(g)}$ (Liu and Fei, 2006; Sachan et al., 2007; Song et al., 2009; Katayama et al., 2010; Arai et al., 2012). Moreover, the included $CH_{4(g)}$ has been taken as evidence for reduced fluid activity in mantle rocks. In contrast, the present study provides evidence that $CH_{4(g)}$ included in the Yushigou orogenic harzburgite has an in situ origin. It is possible that $CH_{4(g)}$ in fluid inclusions investigated in previous studies has an exotic origin that differs from $CH_{4(g)}$ investigated in this study. Alternatively, step-daughter minerals (e.g., serpentine, brucite, and magnetite) might have been neglected during previous petrographic observations and spot Raman analyses on account of their small volumes compared with $CH_{4(g)}$ and their propensity to locally line olivine wall. Re-examination of the petrographies and Raman spectra of previously reported single-phase CH_4-

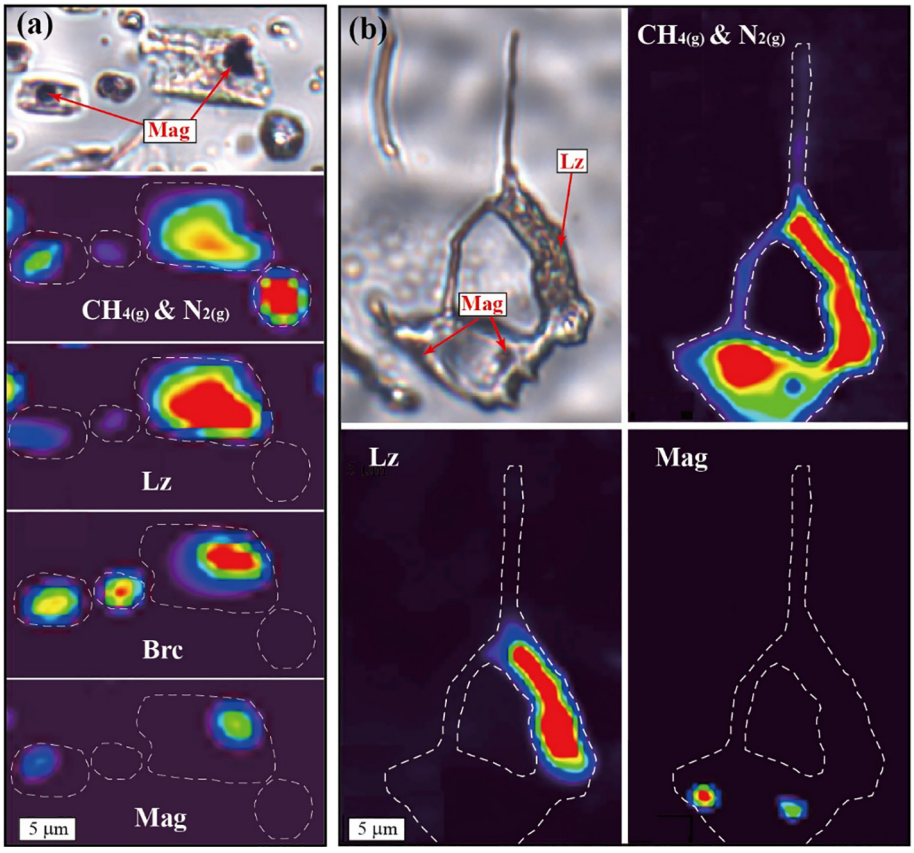

Fig. 7. Hyperspectral Raman mapping of typical (a) brucite-bearing and (b) brucite-absent type II CH_4-bearing fluid inclusions compared with photomicrographs of the mapped fluid inclusions.

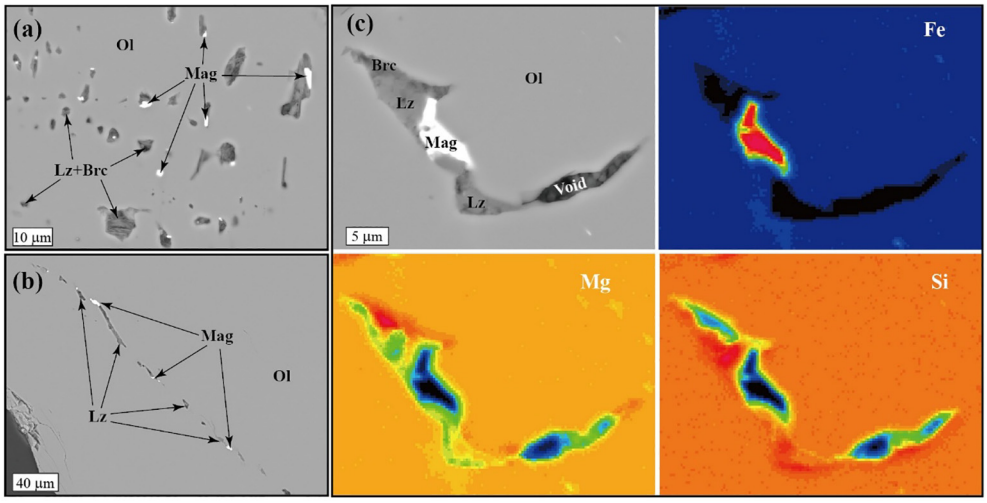

Fig. 8. (a) BSE images of a cluster of brucite-bearing type II CH_4-bearing fluid inclusions. (b) BSE images of a trail of brucite-absent type II CH_4-bearing fluid inclusions. (c) BSE image and element mapping of an opened brucite-bearing type II CH_4-bearing fluid inclusion.

rich fluid inclusions in orogenic peridotite reveals that some fluid inclusions are clearly multiphase and likely contain solid minerals such as magnetite and serpentine (Liu and Fei, 2006; Song et al., 2009). Moreover, serpentinization minerals have already been reported in other olivine-hosted CH_4-bearing fluid inclusions (Katayama et al., 2010; Arai et al., 2012). Therefore, an in situ synthetic origin coupled with internal serpentinization cannot be excluded completely for $CH_{4(g)}$ in these fluid inclusions, which needs to be further verified. Above all, it is suggested

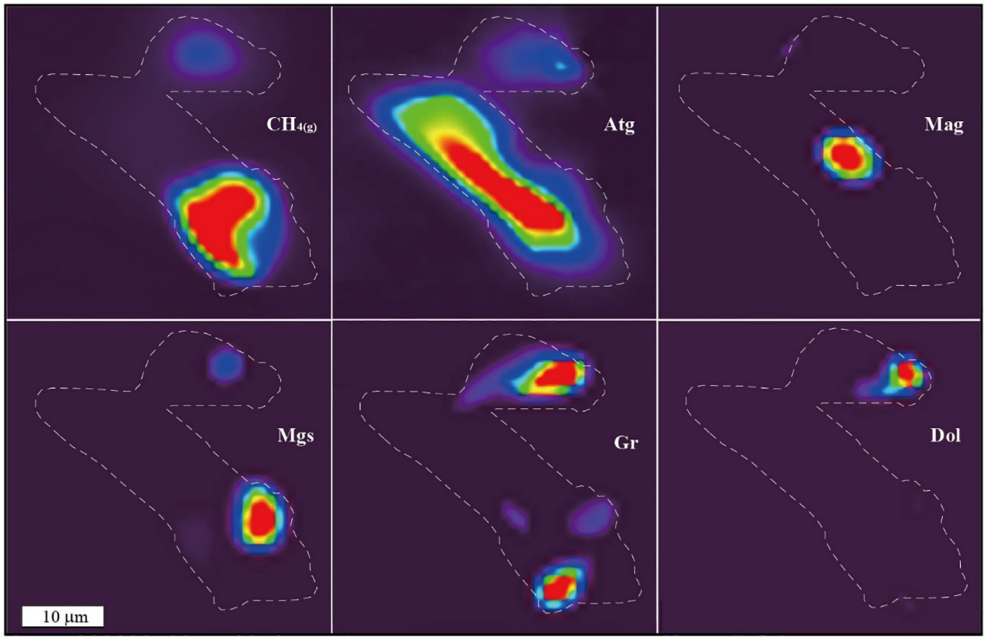

Fig. 9. Hyperspectral Raman mapping of the type III CH_4-bearing fluid inclusion shown in Fig. 2h.

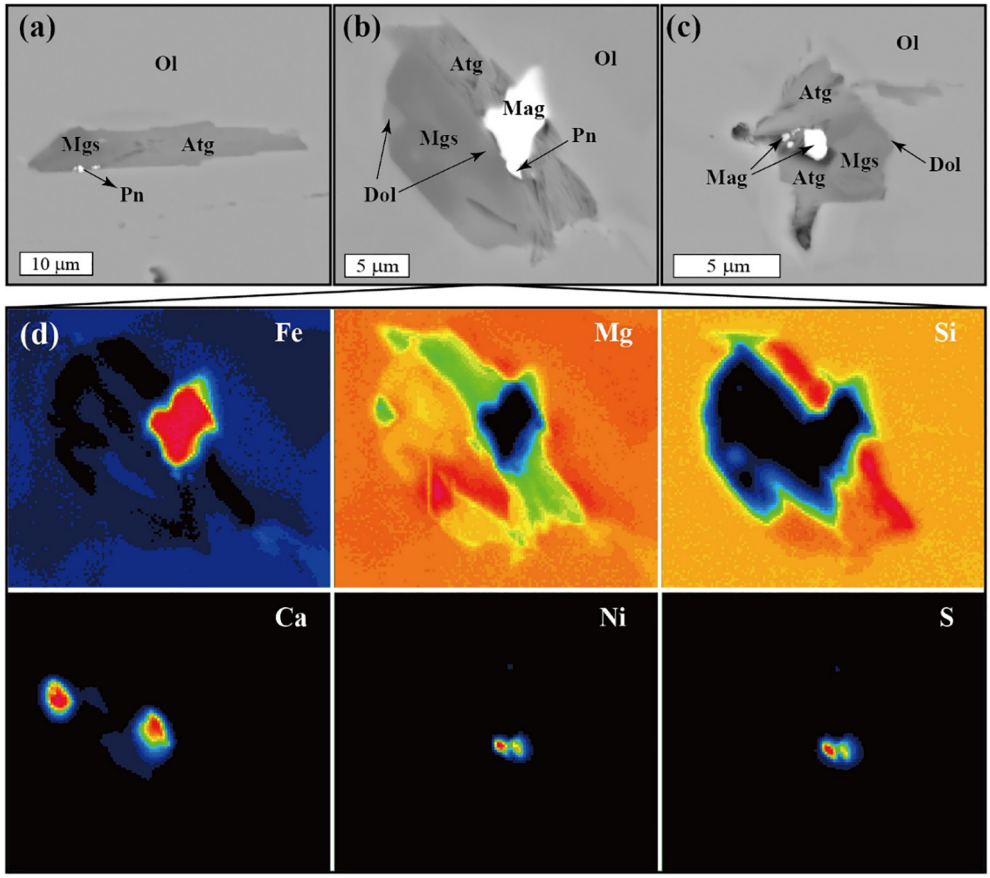

Fig. 10. (a)–(c) BSE images of representative opened type III CH_4-bearing fluid inclusions. (d) Element mapping of the opened fluid inclusion shown in (b).

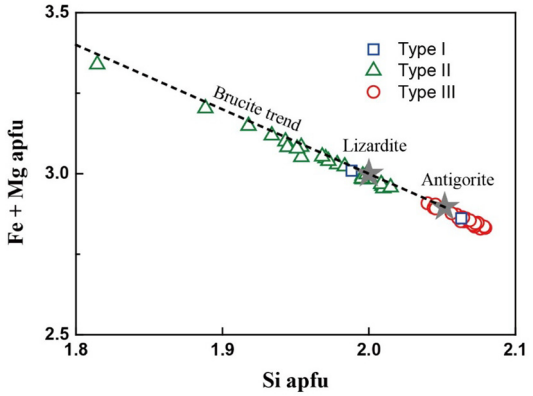

Fig. 11. Plot of Mg + Fe apfu versus Si apfu for serpentine ± brucite in opened CH_4-bearing fluid inclusions. The stars represent ideal lizardite and antigorite without element substitution. The brucite trend indicates intergrowth or mixing with brucite for the analyzed serpentine.

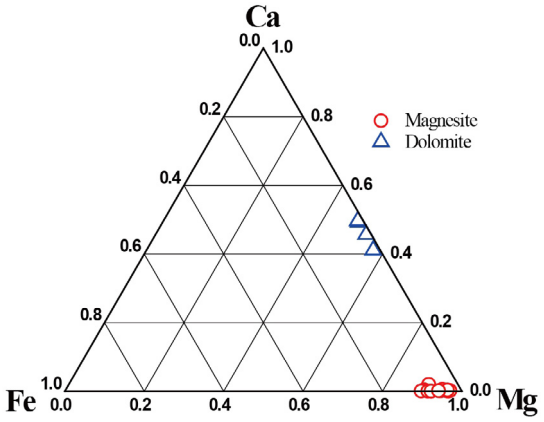

Fig. 12. Ca–Fe–Mg ternary plot for carbonates in opened type III CH_4-bearing fluid inclusions.

that CH_4-bearing fluid inclusions in olivine from orogenic peridotite may not be indicative of reduced mantle conditions unless an internal origin for $CH_{4(g)}$ can be excluded by high-resolution petrological techniques such as Raman mapping.

5.2. High-temperature serpentinization and methanogenesis in type I fluid inclusions

Type I fluid inclusions are mostly prismatic and oriented, occurring in the interior of olivine and aligning parallel to the growth plane of olivine (Figs. 1a–b and 2a–b). Therefore, type I fluid inclusions are probably primary fluid inclusions trapped during the growth of olivine at suprasolidus temperatures of >900–1000 °C. Their pointing in the same direction may be ascribed to plastic deformation under near-solidus conditions (Cao et al., 2015). As the Yushigou harzburgite is typical of forearc mantle peridotite, type I fluid inclusions were thus probably trapped during hydrous melting of the forearc mantle in the presence of ΣCO_2-rich slab fluids (Kawamoto et al., 2013). Therefore, type I fluid inclusions would have formed during the initial stage of subduction when the forearc mantle was hot enough (>900–1000 °C). Serpentinization and associated abiotic CH_4 synthesis could have been initiated in type I fluid inclusions when the forearc mantle cooled down to <600 °C, under which conditions serpentinization can occur.

Compared with lizardite/chrysotile, antigorite is generally considered as the high-temperature form of serpentine (Evans, 2004). Antigorite can form directly from the hydration of olivine via the reaction (Evans, 2004):

$$34Mg_2SiO_4 + 51H_2O = Mg_{48}Si_{34}O_{85}(OH)_{62} + 20Mg(OH)_2.$$
olivine antigorite brucite (4)

Alternatively, antigorite growth due to the breakdown of lizardite/chrysotile is possible at temperatures above 300 °C according to the reaction (Evans, 2004):

$$17Mg_3Si_2O_5(OH)_4 = Mg_{48}Si_{34}O_{85}(OH)_{62} + 3Mg(OH)_2.$$
lizardite/chrysotile antigorite brucite (5)

In addition, antigorite can also be transformed from lizardite/chrysotile by Si metasomatism at temperatures lower than 300 °C via the reaction (Evans, 2004; Klein et al., 2017; Rouméjon et al., 2019):

$$16Mg_3Si_2O_5(OH)_4 + 2SiO_{2(aq)} = Mg_{48}Si_{34}O_{85}(OH)_{62} + H_2O.$$
lizardite/chrysotile antigorite (6)

Antigorite growth from lizardite/chrysotile is also common at elevated ΣCO_2, and is actually due to reaction (6) with the release of excess $SiO_{2(aq)}$ accompanying substantial Mg removal during precipitation of magnesite (Menzel et al., 2018; Boskabadi et al., 2020). Antigorite and brucite in type I fluid inclusions could form directly from olivine via reaction (4), or through a two-step process involving metastable lizardite/chrysotile, given the slow growth kinetics of antigorite (Evans, 2004). In the latter case, reactions in type I fluid inclusions involved initial hydration of olivine into metastable lizardite/chrysotile and brucite via the following reaction:

$$2Mg_2SiO_4 + 3H_2O = Mg_3Si_2O_5(OH)_4 + Mg(OH)_2,$$
olivine lizardite/chrysotile brucite (7)

followed by slower recrystallization of lizardite/chrysotile into antigorite via reaction (5) or (6). However, reaction (5) can hardly occur in cooling static fluid inclusions, as overheating and deformation are probably needed to overcome the very small driving force of this reaction (Evans, 2004; Früh-Green et al., 2001; Zhang et al., 2019b). The presence of brucite in type I fluid inclusions renders reaction (6) unlikely, as brucite crystallization is inhibited if $SiO_{2(aq)}$ is enriched (Klein et al., 2009, 2013; McCollom and Bach, 2009). Therefore, the coexistence of antigorite and brucite in type I fluid inclusions implies direct hydration of olivine by reaction (4). This reaction has been rarely investigated in the literature. However, its back-reaction

$$Mg_{48}Si_{34}O_{85}(OH)_{62} + 20Mg(OH)_2 = 34Mg_2SiO_4 + 51H_2O \quad (8)$$

antigorite brucite olivine

is well known in metamorphic petrology, as it is responsible for the onset of antigorite dehydration and the first occurrence of secondary olivine in subducted serpentinite (Scambelluri et al., 2004; Bretscher et al., 2018). Reaction (8) is constrained to take place mostly at 400–500 °C (Wunder and Schreyer, 1997; Evans, 2004; Bretscher et al., 2018). Therefore, the alteration of olivine in type I fluid inclusions via reaction (4) could have started at relatively high temperatures (400–500 °C) in the stability field of antigorite.

Previous studies focusing on serpentinization at 50 MPa have suggested that serpentinization is extremely limited and olivine is stable at temperatures > 400 °C (Allen and Seyfried, 2003; Klein et al., 2009, 2013, 2019; McCollom and Bach, 2009). In this respect, serpentinization-related production of H_2 and synthesis of CH_4 are unlikely above 400 °C at pressures up to 50 MPa. Compared with lizardite/chrysotile, antigorite has a much higher thermal and barometric stability that enables serpentinization at 400–600 °C in deep mantle rocks (Evans, 2010). Nevertheless, there is uncertainty as to whether antigorite serpentinization can precipitate magnetite, evolve H_2, and synthesize CH_4 (Evans, 2010). Type I fluid inclusions in the Yushigou harzburgite indicate that magnetite can be generated during hydration of Fe-bearing olivine into antigorite, along with reduction of H_2O into $H_{2(g)}$ and further synthesis of $CH_{4(g)}$ from ΣCO_2. The feasibility of magnetite precipitation during antigorite serpentinization is also indirectly supported by the fact that considerable magnetite can participate in reaction (8) to produce Fe-rich secondary olivine in subducted serpentinite (Scambelluri et al., 1991; Debret et al., 2013). However, the reaction sequence of serpentinization in the stability field of antigorite, including the partitioning of Fe into brucite and the precipitation of magnetite, is currently poorly understood. Limited EPMA data and element mapping show that brucite can retain considerable amounts of Fe during antigorite serpentinization (Figs. 5 and 11), which is similar to the case of lizardite/chrysotile serpentinization (Klein et al., 2009, 2013, 2019; McCollom and Bach, 2009). Hydration of olivine into antigorite and Fe-rich brucite without the precipitation of magnetite has also been reported previously (Beard et al., 2009). Therefore, the thermodynamics of Fe partitioning during antigorite serpentinization need to be better constrained in the future.

Overall, type I fluid inclusions in the Yushigou harzburgite demonstrate that substantial oxidation of ferrous Fe in olivine and coupled formation of H_2 and CH_4 are thermodynamically favorable during hydration of olivine into antigorite. The high thermal and barometric stability of antigorite (Wunder and Schreyer, 1997; Evans, 2004, 2010) tentatively suggests that abiotic CH_4 synthesis associated with serpentinization can occur to considerable depths. Subduction zones, including subducted lithospheric mantle and the forearc mantle wedge, are potential sites of such deep formation of serpentinization-related abiotic CH_4. Extensive production of high-pressure abiotic $CH_{4(g)}$ has already been reported in metamorphosed ophicarbonate from the Italian Alps (Vitale Brovarone et al., 2017). Abundant CH_4-bearing inclusions in the subducted Alpine ophicarbonate are considered to have formed from the reduction of carbonates by $H_{2(g)}$ produced during antigorite serpentinization of surrounding peridotite. Antigorite serpentinization is more prevalent in the deep forearc mantle (Evans, 2010), compared with subducted slab. Therefore, widespread abiotic synthesis of CH_4 is expected to occur in the forearc mantle in the presence of ΣCO_2-bearing slab fluids, if kinetic barriers can be overcome. This process may contribute to deep-sourced CH_4 in the forearc area, with the potential to support deep chemosynthetic microbial activity (Plümper et al., 2017). Overall, CH_4 abiogenesis coupled with antigorite serpentinization may play an important role in redox transfer, carbon cycling, and vital activity in subduction zones, which is probably underestimated at present.

5.3. Silica control on serpentinization and methanogenesis in type II fluid inclusions

Type II fluid inclusions are distributed mostly in intragranular trails, planes, and patches (Fig. 1c–f). Therefore, they have a secondary origin, involving entrapment of external fluids along annealed fractures. Trails of type II fluid inclusions are locally crosscut by serpentine veinlets in the matrix, indicating entrapment of fluid inclusions before the infiltration of fluids at the low-temperature stage when olivine could not anneal. Although some type II fluid inclusions show weak preferred orientations and display negative crystal shapes (Fig. 1e and 2d), a primary origin is not favored for them as they have similar compositions to those of other type II fluid inclusions with a clearly secondary origin. In particular, all type II fluid inclusions are characterized by the presence of $N_{2(g)}$ (Fig. 3e and f), which remained inert during internal serpentinization while ΣCO_2 was reduced to $CH_{4(g)}$. Nitrogen-bearing fluids can be derived from air-equilibrated pore fluids trapped in sediments, metamorphism of N-bearing sediments, or deep lithosphere degassing of N_2 with an igneous or mantle origin (Vacquand et al., 2018). As the Yushigou harzburgite represents typical forearc mantle peridotite, subducted sediments are thus the preferred source of ΣCO_2- and N_2-bearing fluids in type II fluid inclusions. Although fluids in type II fluid inclusions were also derived from subducting slab, type II fluid inclusions would have formed at lower temperatures (<400–500 °C) during a later stage than type I fluid inclusions, as they, unlike type I fluid inclusions, were not subjected to high-temperature antigorite serpentinization.

As mentioned above, type II fluid inclusions can be divided into brucite-bearing and brucite-free subtypes. Methane in brucite-free type II fluid inclusions has smaller Raman υ1 band than $CH_{4(g)}$ in brucite-bearing fluid inclusions (Fig. 6b). Although $N_{2(g)}$ can decrease the Raman shift of the $CH_{4(g)}$ υ1 band (Fabre and Oksengorn, 1992; Seitz et al., 1993), the calculated partial pressure for $CH_{4(g)}$ in type II fluid inclusions should not be significantly

influenced, as only minor $N_{2(g)}$ is present in type II fluid inclusions. Therefore, the vapor pressure of $CH_{4(g)}$ in brucite-free type II fluid inclusions is likely higher than that of $CH_{4(g)}$ in brucite-bearing type II fluid inclusions. In other words, CH_4 productivity in brucite-bearing type II fluid inclusions is lower than that in brucite-free type II fluid inclusions. The contrast is probably dictated by brucite, as brucite can take up considerable ferrous Fe during serpentinization (Klein et al., 2009, 2013, 2019; McCollom and Bach, 2009). Less Fe would be oxidized if considerable ferrous Fe was hosted by brucite, yielding less $H_{2(g)}$ and consequently $CH_{4(g)}$. The uptake of iron by brucite is supported by the EPMA results, which reveal that lizardite with significant brucite intergrowth (low Si apfu and high Fe + Mg apfu in Fig. 11) is enriched in FeO (Table S2).

Excess $SiO_{2(aq)}$ is required for brucite to be eliminated from the products of olivine hydration by the reaction:

$$3Mg(OH)_2 + 2SiO_{2(aq)} = Mg_3Si_2O_5(OH)_4 + H_2O. \quad (9)$$

brucite lizardite/chrysotile

Consequently, the simplest explanation for the contrast between brucite-free and brucite-bearing type II fluid inclusions is that brucite-free inclusions originally contained elevated amounts of $SiO_{2(aq)}$. However, brucite is also unstable during serpentinization under fluid-dominated conditions even if the fluids contain only minor $SiO_{2(aq)}$. Previous petrological observations of serpentinized peridotite have revealed that hydration of olivine produces serpentine and brucite under rock-dominated conditions, followed by breakdown of early-formed brucite into magnetite and serpentine under water-dominated conditions (Bach et al., 2004, 2006; Frost et al., 2013). Nevertheless, fluid/mineral ratios during internal serpentinization in fluid inclusions are very low, given the small volumes of fluid inclusions and large amounts of host olivine. In other words, internal serpentinization in fluid inclusions is always mineral-dominated. Therefore, the formation of brucite-free type II fluid inclusions is likely ascribed to elevated concentrations of $SiO_{2(aq)}$ in the trapped fluids. Brucite-free type II fluid inclusions with large sizes were created during this stage of Si-enriched fluid activity. These large fluid inclusions were more easily subjected to re-equilibration during late-stage evolution owing to a threshold size effect for re-equilibration of fluid inclusions (Bodnar, 2003; Campione, 2018), which may explain their irregular morphologies with cuspate endings and stretching tentacles.

5.4. Serpentinization and methanogenesis with elevated ΣCO_2 in type III fluid inclusions

Type III fluid inclusions are generally similar to type II fluid inclusions in distribution. They also occur along trails, planes, and patches (Fig. 1g–i), which indicates a secondary origin. Planes of type II fluid inclusions are locally crosscut by planes of type III fluid inclusions, suggesting that type III fluid inclusions formed later than type II fluid inclusions. However, the grading of type II fluid inclusions into type III fluid inclusions implies that types II and III fluid inclusions actually record continuous fluid fluxes into the Yushigou harzburgite. Therefore, different constituents of types II and III fluid inclusions may reflect the compositional evolution of percolating fluids from N_2-rich and ΣCO_2-poor to N_2-poor and ΣCO_2-rich. In addition, the presence of dolomite in type III fluid inclusions reveals that the fluids became enriched in Ca^{2+}.

As types II and III fluid inclusions initially formed in a tight sequence, internal serpentinization in both types of fluid inclusions should have proceeded at similar temperatures. However, antigorite was produced in type III fluid inclusions, in contrast to lizardite in type II fluid inclusions. It is unlikely that antigorite in type III fluid inclusions was produced via reaction (4), as in this case, antigorite should also have been produced in type II fluid inclusions. Instead, elevated ΣCO_2 in type III fluid inclusions was probably responsible for the stability of antigorite. Therefore, internal serpentinization in types II and III fluid inclusions is roughly estimated to have occurred at about the critical temperature (~250–300 °C) of lizardite breakdown into antigorite (Evans, 2004). At this temperature, lizardite is stable in type II fluid inclusions, whereas elevated ΣCO_2 ensures the stability of antigorite in type III fluid inclusions.

Alteration of olivine at elevated ΣCO_2 involves rapid carbonation and slower serpentinization of olivine (Jones et al., 2010; Klein and McCollom, 2013; Lafay et al., 2014; Grozeva et al., 2017). In this regard, excess $SiO_{2(aq)}$ could be released during fast magnesite precipitation in type III fluid inclusions according to the reaction (Grozeva et al., 2017):

$$Mg_2SiO_4 + 2\Sigma CO_2 = 2MgCO_3 + SiO_{2(aq)}. \quad (10)$$

olivine magnesite

Dolomite could be precipitated if Ca^{2+} participated in the reaction. Excess $SiO_{2(aq)}$ released by reaction (10) would suggest that antigorite should be the most stable serpentine phase in type III fluid inclusions. However, rare lizardite identified in type III fluid inclusions (Fig. S5) suggests that serpentinization in type III fluid inclusions was probably a two-step process, with initial hydration of olivine into lizardite via reaction (7) followed by breakdown of lizardite into antigorite via reaction (6). This two-step process is consistent with the sluggish nucleation kinetics of antigorite (Evans, 2004), favoring the initial formation of metastable lizardite prior to its recrystallization to stable antigorite. Brucite produced in type III fluid inclusions probably reacted out, as brucite is more reactive than lizardite/chrysotile during olivine carbonation (Klein and Garrido, 2011; Klein and McCollom, 2013; Grozeva et al., 2017). In contrast to the ubiquitous occurrence of antigorite in type III fluid inclusions, antigorite has not been reported in previous experimental studies on serpentinization in the presence of ΣCO_2-rich fluids (Jones et al., 2010; Klein and McCollom, 2013; Lafay et al., 2014; Grozeva et al., 2017). This may be partly ascribed to the small thermodynamic driving force required to form antigorite from lizardite/chrysotile (Evans, 2004), which kinetically inhibits the growth of antigorite over the timescale of experiments. In contrast, antigorite growth at the expense of lizardite/chrysotile could be achieved in type III fluid inclusions and natural carbonated serpentinite (Menzel et al., 2018;

Boskabadi et al., 2020) over a much longer timescale, probably in the order of tens of years (Beinlich et al., 2020). Nevertheless, further studies are needed to clarify the growth kinetics of antigorite.

Previous experimental investigations have shown that serpentinization ceases in the presence of high concentrations of ΣCO_2 (Klein and McCollom, 2013; Grozeva et al., 2017), impeding the production of H_2 and consequently CH_4. In this respect, ferrous Fe in olivine is rapidly incorporated into carbonate without oxidation into ferric Fe. Carbonates in type III fluid inclusions do contain considerable Fe (Fig. 12; Table S2). However, the presence of magnetite in type III fluid inclusions indicates that some Fe has undergone oxidation, facilitating the generation of $H_{2(g)}$ and synthesis of $CH_{4(g)}$. Therefore, it is suggested that ΣCO_2 concentrations in type III fluid inclusions were not sufficiently high to allow exclusive incorporation of ferrous Fe into carbonates. Some experimental studies have also shown that magnetite is precipitated at lower ΣCO_2 concentrations than those in the abovementioned experiments (Jones et al., 2010; Lafay et al., 2014). Nevertheless, CH_4 productivity in type III fluid inclusions should be lower than that in brucite-free type II fluid inclusions, as considerable ferrous Fe was taken up by carbonates. This is supported by the generally lower vapor pressure of $CH_{4(g)}$ in type III fluid inclusions compared with that in brucite-free type II fluid inclusions (Fig. 6). In contrast, the partial pressure of $CH_{4(g)}$ in type III fluid inclusions is higher than that in brucite-bearing type II fluid inclusions, revealing that brucite can be more efficient than carbonates in taking up ferrous iron during serpentinization. Partial pressure of $CH_{4(g)}$ in type I fluid inclusions is similar to that of type III fluid inclusions, indicating that CH_4 yield in type I fluid inclusions was also diminished due to incorporation of ferrous iron into carbonate. Nevertheless, the original ΣCO_2 concentrations in type I fluid inclusions should be lower than those in type III fluid inclusions, as brucite is stable in type I fluid inclusions.

5.5. Implications for serpentinization and associated abiotic CH_4 synthesis

The presence and nature of CH_4-bearing fluid inclusions in olivine from the Yushigou harzburgite demonstrate the following: (1) orogenic peridotite can contain large quantities of endogenetic $CH_{4(g)}$ within olivine-hosted fluid inclusions; (2) nitrogen can remain stable during serpentinization and be an important component of CH_4-bearing fluid inclusions in orogenic peridotite; and (3) $CH_{4(g)}$ included in fluid inclusions in orogenic peridotite can be preserved for a long time, considering that the Yushigou ophiolite formed in the Cambrian (Song et al., 2013). The dense distribution of multiple types of CH_4-bearing fluid inclusions in the Yushigou harzburgite (Figs. 1 and 2) supports that CH_4-bearing fluid inclusions can be very abundant in orogenic peridotite (Klein et al., 2019; Grozeva et al., 2020). Given the forearc origin of the Yushigou harzburgite (Song et al., 2009; Zhang et al., 2019a), the unusual enrichment of CH_4-bearing fluid inclusions in the Yushigou harzburgite may be attributable to the prolonged flux of slab fluids into the mantle wedge. In this regard, olivine-hosted fluid inclusions in SSZ peridotite may be a significant reservoir of abiotic CH_4 in both present and fossil mantle wedge. Leaching of these CH_4-bearing fluid inclusions in SSZ peridotite, such as that in the Mariana forearc, Oman ophiolite, and New Caledonia ophiolite, may therefore contribute greatly to the CH_4 flux in related hydrothermal fields (Klein et al., 2019; Grozeva et al., 2020), even if $CH_{4(g)}$ included in the peridotite cannot completely account for CH_4 venting at relevant sites. Besides, $N_{2(g)}$ trapped in CH_4-bearing fluid inclusions can also be released during leaching, which can account for $N_{2(g)}$ present in reduced gas seepages in many ophiolitic complexes (Vacquand et al., 2018). Moreover, leaching of $CH_{4(g)}$ and $N_{2(g)}$ included in orogenic peridotite can last over an extended period of geological time, given the effectiveness of $CH_{4(g)}$ and $N_{2(g)}$ storage in olivine-hosed fluid inclusions.

More importantly, CH_4-bearing fluid inclusions in the Yushigou harzburgite demonstrate that olivine-hosted CH_4-bearing fluid inclusions in orogenic peridotite can provide a novel avenue for studying abiotic CH_4 synthesis during serpentinization. The presence of multiple types of olivine-hosted CH_4-bearing fluid inclusions in the Yushigou harzburgite demonstrates that CH_4-bearing fluid inclusions can record olivine–fluid interaction equilibrated under different conditions, including temperature, $SiO_{2(aq)}$ content, and ΣCO_2 concentration, etc. Olivine-hosted fluid inclusions constitute an efficient container of gaseous CH_4 synthesized during internal serpentinization, and can retain $H_{2(g)}$ if the conditions are favorable. Moreover, olivine-hosted fluid inclusions are well equilibrated owing to the sufficiently long durations of internal serpentinization, varying from several months to over 1 million years with a dependence on temperature, inclusion size, and fluid chemistry (Lamadrid et al. 2020). In contrast, natural serpentinite was separated from any gas phase produced during serpentinization by actively percolating fluids. Experimental synthesis of CH_4 during serpentinization suffers from background contamination and kinetic barriers (McCollom, 2013, 2016). Theoretical predictions of serpentinization-driven CH_4 formation can deviate from natural situations because of simplification of systems and inadequate knowledge of mineral thermodynamic data. Therefore, olivine-hosted CH_4-bearing fluid inclusions in orogenic peridotite have an advantage over simulations, experiments, and serpentinite rocks in providing new insights into abiogenesis of CH_4 during serpentinization. For example, CH_4-bearing fluid inclusions in the Yushigou harzburgite presented in this study support the idea that antigorite may play an important role during methanogenesis associated with serpentinization at high temperatures and elevated ΣCO_2 concentrations. Future investigations into more diverse CH_4-bearing fluid inclusions in olivine from other orogenic peridotites are expected to further our understanding of serpentinization and associated abiotic CH_4 synthesis. A disadvantage of investigating olivine-hosted CH_4-bearing fluid inclusions may be the minute sizes of fluid inclusions, which could hinder extraction of some petrological and geochemical information, although this potential problem can be partly avoided by using high-resolution in situ analyses.

6. CONCLUSION

This study investigated the genesis of $CH_{4(g)}$ included in olivine-hosted fluid inclusions in ophiolitic peridotite from the North Qilian orogen, northern Tibet. Multiple types of CH_4-bearing fluid inclusions were identified in the peridotite, revealing in situ CH_4 synthesis via reduction of ΣCO_2 by $H_{2(g)}$ produced during diverse internal serpentinization within fluid inclusions. Serpentinization and associated abiotic CH_4 synthesis in primary type I fluid inclusions occurred at high temperatures, with the hydration of olivine directly into antigorite, brucite, and magnetite. This not only refutes the previous paradigm suggesting inhibited H_2 and CH_4 production during high-temperature antigorite serpentinization, but also expands the realm of serpentinization-associated CH_4 synthesis to greater depths. In contrast, abiotic CH_4 synthesis was associated with lizardite serpentinization at lower temperatures in type II fluid inclusions. Type II fluid inclusions are divided into brucite-bearing and brucite-free subtypes, with the crystallization of brucite or not determined by the content of dissolved silica in trapped fluids. Moreover, CH_4 productivity in brucite-bearing type II fluid inclusions is lower than that of brucite-free type II fluid inclusions, indicating that brucite can diminish the CH_4 yield by taking up considerable ferrous iron during serpentinization. Serpentinization and associated abiotic CH_4 synthesis in type III fluid inclusions were completed under similar temperatures to those applying to type II fluid inclusions. However, elevated ΣCO_2 in type III fluid inclusions indicates that antigorite is favored as the stable serpentine phase when carbonate is saturated. Moreover, a two-step process for antigorite growth during serpentinization at elevated ΣCO_2, namely, hydration of olivine into lizardite followed by transformation of lizardite into antigorite, is revealed by the presence of relict lizardite in type III fluid inclusions. Overall, the unusual abundance of CH_4-bearing fluid inclusions in the Yushigou harzburgite demonstrates that CH_4-bearing fluid inclusions in orogenic peridotite can be a significant reservoir of abiotic CH_4 in fossil orogens. More importantly, our analyses of multiple types of CH_4-bearing fluid inclusions in the Yushigou harzburgite, which record diverse serpentinization and associated abiotic methanogenesis under different conditions, demonstrate that the study of olivine-hosted CH_4-bearing fluid inclusions can provide new insights into serpentinization and associated abiotic CH_4 synthesis.

Declaration of Competing Interest

The authors declare that they have no known competing financial interests or personal relationships that could have appeared to influence the work reported in this paper.

ACKNOWLEDGEMENTS

This study was supported by funds from the Second Tibetan Plateau Scientific Expedition and Research (2019QZKK0702), the Strategic Priority Research Program of the Chinese Academy of Sciences (XDB41000000, XDB42020403, and XDA2007030402), the Key Program of the Chinese Academy of Sciences (QYZDJ-SSW-DQC026), the Tuguangchi Award for Excellent Young Scholar (GIGCAS), and the Natural Science Foundation of China (42021002, 41703029, 91855215, and 41630208). We thank Qing-Yun Jiang and Guo-Rong Tang for help in the field, and Hai-Bo Yan and Jian Di for help with the Raman analyses. This manuscript benefits greatly from the thorough reviews by N. G. Grozeva, Shoji Arai, and R. J. Bodnar, as well as the editorial work and review of the associate editor Frieder Klein. This is contribution No. IS-2958 from GIGCAS.

APPENDIX A. SUPPLEMENTARY MATERIAL

Supplementary data to this article can be found online at https://doi.org/10.1016/j.gca.2020.12.016.

REFERENCES

Allen D. E. and Seyfried, Jr., W. E. (2003) Compositional controls on vent fluids from ultramafic-hosted hydrothermal systems at mid-ocean ridges: An experimental study at 400°C, 500 bars. *Geochim. Cosmochim. Acta* **67**(8), 1531–1542.

Andreani M. and Ménez B. (2019) New perspectives on abiotic organic synthesis and processing during hydrothermal alteration of the oceanic lithosphere. In *Deep Carbon: Past to Present* (eds. B. Orcutt, I. Daniel and R. Dasgupta). Cambridge University Press, Cambridge, pp. 447–479.

Arai S., Ishimaru S. and Mizukami T. (2012) Methane and propane micro-inclusions in olivine in titanoclinohumite-bearing dunites from the Sanbagawa high-P metamorphic belt, Japan: Hydrocarbon activity in a subduction zone and Ti mobility. *Earth Planet. Sci. Lett.* **353–354**, 1–11.

Bach W., Garrido C. J., Harvey J., Paulick H. and Rosner M. (2004) Variable seawater-peridotite interactions: first insights from ODP Leg 209, MAR 15°N. *Geochem. Geophys. Geosyst.* **5**, Q09F26.

Bach W., Paulick H., Garrido C. J., Ildefonse B., Meurer W. P. and Humphris S. E. (2006) Unraveling the sequence of serpentinization reactions: petrography, mineral chemistry, and petrophyscis of serpentinites from MAR 15°N (ODP Leg 209, Site 1274). *Geophys. Res. Lett.* **33**, L13306.

Beard J. S., Frost B. R., Fryer P., McCaig A., Searle R., Ildefonse B., Zinin P. and Sharma S. K. (009) Onset and progression of serpentinization and magnetite formation in olivine-rich troctolite from IODP Hole U1309D. *J. Petrol.* **50**, 387–403.

Beinlich A., John T., Vrijmoed J. C., Tominaga M., Magna T. and Podladchikov Y. Y. (2020) Instantaneous rock transformations in the deep crust driven by reactive fluid flow. *Nat. Geosci.* **13**, 307–311.

Beyssac O. and Lazzeri M. (2012) Application of Raman spectroscopy to the study of graphitic carbons in the Earth sciences. In *Applications of Raman spectroscopy to Earth sciences and cultural heritage* (eds. Dubessy J., Caumon M. - C. and Rull F.). *EMU Notes Mineral* **12**, 415–454.

Bodnar R. J. (2003) Reequilibration of fluid inclusions. In *Fluid Inclusions: Analysis and Interpretation* (eds. Samson I., Anderson A. and Marshall D.). *Mineral Assoc. Canada, Short Course* **32**, 213–230.

Boskabadi A., Pitcairn I. K., Leybourne M. I., Teagle D. A. H., Cooper M. J., Hadizadeh H., Nasiri Bezenjani R. and Monazzami Bagherzadeh R. (2020) Carbonation of ophiolitic ultramafic rocks: Listvenite formation in the Late Cretaceous ophiolites of eastern Iran. *Lithos* **352–353**, 105307.

Bretscher A., Hermann J. and Pettke T. (2018) The influence of oceanic oxidation on serpentinite dehydration during subduction. *Earth Planet. Sci. Lett.* **499**, 173–184.

Cao Y., Jung H., Song S., Park M., Jung S. and Lee J. (2015) Plastic deformation and seismic properties in fore-arc mantles: A petrofabric analysis of the Yushigou harzburgites, North Qilian suture zone, NW China. *J. Petrology* **56**(10), 1897–1944.

Campione M. (2018) Threshold effects for the decrepitation and stretching of fluid inclusions. *J. Geophys. Res. Solid Earth* **123** (5), 3539–3548.

Debret B., Nicollet C., Andreani M., Schwartz S. and Godard M. (2013) Three steps of serpentinization in an eclogitized oceanic serpentinization front (Lanzo Massif-Western Alps). *J. Metamorph. Geol.* **31**, 165–186.

Etiope G. and Schoell M. (2014) Abiotic gas: atypical, but not rare. *Elements* **10**(4), 291–296.

Etiope G. and Whiticar M. J. (2019) Abiotic methane in continental ultramafic rock systems: Towards a genetic model. *Appl. Geochem.* **102**, 139–152.

Evans B. W. (2004) The serpentinite multisystem revisited: chrysotile is metastable. *Int. Geol. Rev.* **46**, 479–506.

Evans B. W. (2010) Lizardite versus antigorite serpentinite: magnetite, hydrogen, and life(?). *Geology* **38**, 879–882.

Evans B. W., Hattori K. and Baronnet A. (2013) Serpentinite: what, why, where? *Elements* **9**(2), 99–106.

Fabre D. and Oksengorn B. (1992) Pressure and density dependence of the CH_4 and N_2 Raman lines in an equimolar CH_4 /N_2 gas mixture. *Appl. Spectrosc.* **46**(3), 468–471.

Frezzotti M. L., Tecce F. and Casagli A. (2012) Raman spectroscopy for fluid inclusion analysis. *J. Geochem. Explor.* **112**, 1–20.

Frost B. R., Evans K. A., Swapp S. M., Beard J. S. and Mothersole F. E. (2013) The process of serpentinization in dunite from New Caledonia. *Lithos* **178**, 24–39.

Früh-Green G. L., Scambelluri M. and Vallis F. (2001) O–H isotope ratios of high pressure ultramafic rocks: implications for fluid sources and mobility in the subducted hydrous mantle. *Contrib Mineral Petrol* **141**(2), 145–159.

Grozeva N. G., Klein F., Seewald J. S. and Sylva S. P. (2017) Experimental study of carbonate formation in oceanic peridotite. *Geochim. Cosmochim. Acta* **199**, 264–286.

Grozeva N. G., Klein F., Seewald J. S. and Sylva S. P. (2020) Chemical and isotopic analyses of hydrocarbon-bearing fluid inclusions in olivine-rich rocks. *Phil. Trans. R. Soc. A* **378**, 20180431.

Hall D. L. and Bodnar R. J. (1990) Methane in fluid inclusions from granulites: A product of hydrogen diffusion? *Geochim. Cosmochim. Acta* **54**, 641–651.

Hall D. L., Bodnar R. J. and Craig J. R. (1991) Evidence for postentrapment diffusion of hydrogen into peak metamorphic fluid inclusions from the massive sulfide deposits at Ducktown, Tennessee. *Am. Mineral.* **76**, 1344–1355.

Jones L. C., Rosenbauer R., Goldsmith J. I. and Oze C. (2010) Carbonate control of H_2 and CH_4 production in serpentinization systems at elevated P-Ts. *Geophys. Res. Lett.* **37**(14), L14306.

Katayama I., Kurosaki I. and Hirauchi K.-I. (2010) Low silica activity for hydrogen generation during serpentinization: An example of natural serpentinites in the Mineoka ophiolite complex, central Japan. *Earth Planet. Sci. Lett.* **298**(1–2), 199–204.

Kawamoto T., Yoshikawa M., Kumagai Y., Mirabueno M. H. T., Okuno M. and Kobayashi T. (2013) Mantle wedge infiltrated with saline fluids from dehydration and decarbonation of subducting slab. *Proc. Natl. Acad. Sci.* **110**, 9663–9668.

Kelley D. S. (1996) Methane-rich fluids in the oceanic crust. *J. Geophys. Res. Solid Earth* **101**, 2943–2962.

Kelley D. S. and Früh-Green G. L. (1999) Abiogenic methane in deep-seated mid-ocean ridge environments: insights from stable isotope analyses. *J. Geophys. Res. Solid Earth* **104**, 10439–10460.

Kelley D. S. and Früh-Green G. L. (2001) Volatile lines of descent in submarine plutonic environments: insights from stable isotope and fluid inclusion analyses. *Geochim. Cosmochim. Acta* **65**(19), 3325–3346.

Klein F., Bach W., Jöns N., McCollom T. M., Moskovitz B. and Berquo T. (2009) Iron partitioning and hydrogen generation during serpentinization of abyssal peridotites from 15°N on the Mid-Atlantic Ridge. *Geochim. Cosmochim. Acta* **73**, 6868–6893.

Klein F. and Garrido C. J. (2011) Thermodynamic constraints on mineral carbonation of serpentinized peridotite. *Lithos* **126**(3–4), 147–160.

Klein F., Bach W. and McCollom T. M. (2013) Compositional controls on hydrogen generation during serpentinization of ultramafic rocks. *Lithos* **178**, 55–69.

Klein F. and McCollom T. M. (2013) From serpentinization to carbonation: new insights from a CO_2 injection experiment. *Earth Planet. Sci. Lett.* **379**, 137–145.

Klein F., Marschall H. R., Bowring S. A., Susan E. H. and Gregory H. (2017) Mid-ocean ridge serpentinite in the Puerto Rico trench: from seafloor spreading to subduction. *J. Petrol.* **58**, 1729–1754.

Klein F., Grozeva N. G. and Seewald J. S. (2019) Abiotic methane synthesis and serpentinization in olivine-hosted fluid inclusions. *Proc. Natl. Acad. Sci.* **116**, 17666–17672.

Klein F., Tarnas J. and Bach W. (2020) Abiotic sources of molecular hydrogen on Earth. *Elements* **16**, 19–24.

Lafay R., Montes-Hernandez G., Janots E., Chiriac R., Findling N. and Toche F. (2014) Simultaneous precipitation of magnesite and lizardite from hydrothermal alteration of olivine under high-carbonate alkalinity. *Chem. Geol.* **368**, 63–75.

Lamadrid H. M., Zajacz Z., Klein F. and Bodnar R. J. (2020) Synthetic fluid inclusions XXIII. Effect of temperature and fluid composition on rates of serpentinization of olivine. *Geochim. Cosmochim. Acta* **292**, 285–308.

Liu W. and Fei P. X. (2006) Methane-rich fluid inclusions from ophiolitic dunite and post-collisional mafic-ultramafic intrusion: the mantle dynamics beneath the Paleo-Asian Ocean through to the post-collisional period. *Earth Planet. Sci. Lett.* **242**, 286–301.

Lu W., Chou I. M., Burruss R. C. and Song Y. (2007) A unified equation for calculating methane vapor pressures in the CH_4-H_2O system with measured Raman shifts. *Geochim. Cosmochim. Acta* **71**, 3969–3978.

Mavrogenes J. A. and Bodnar R. J. (1994) Hydrogen movement into and out of fluid inclusions in quartz-Experimental evidence and geologic implications. *Geochim. Cosmochim. Acta* **58**, 141–148.

McCollom T. M. and Bach W. (2009) Thermodynamic constraints on hydrogen generation during serpentinization of ultramafic rocks. *Geochim. Cosmochim. Acta* **73**, 856–875.

McCollom T. M. (2013) Laboratory simulations of abiotic hydrocarbon formation in Earth's deep subsurface. *Rev. Mineral. Geochem.* **75**, 467–494.

McCollom T. M. and Seewald J. S. (2013) Serpentinites, Hydrogen, and Life. *Elements* **9**(2), 129–134.

McCollom T. M. (2016) Abiotic methane formation during experimental serpentinization of olivine. *Proc. Natl. Acad. Sci.* **113**, 13965–13970.

McCollom T. M., Klein F., Robbins M., Moskowitz B., Berquó T. S., Jöns N., Bach W. and Templeton A. (2016) Temperature

trends for reaction rates, hydrogen generation, and partitioning of iron during experimental serpentinization of olivine. *Geochim. Cosmochim. Acta* **181**, 175–200.

McDermott J. M., Seewald J. S., German C. R. and Sylva S. P. (2015) Pathways for abiotic organic synthesis at submarine hydrothermal fields. *Proc. Natl. Acad. Sci.* **112**, 7668–7672.

Ménez B. (2020) Abiotic hydrogen and methane: fuels for life. *Elements* **16**, 39–46.

Menzel M., Garrido C. J., Sánchez-Vizcaíno V. L. and Marchesi C. (2018) Carbonation of peridotite by CO_2-rich fluids: Listvenite formation in the Advocate Ophiolite (Newfoundland, Canada). *Lithos* **323**, 238–261.

Miura M., Arai S. and Mizukami T. (2011) Raman spectroscopy of hydrous inclusions in olivine and orthopyroxene in ophiolitic harzburgite: implications for elementary processes in serpentinization. *J. Mineral. Petrol. Sci.* **106**, 91–96.

Plümper O., King H. E., Geisler T., Liu Y., Pabst S., Savov I. P., Rost D. and Zack T. (2017) Subduction zone forearc serpentinites as incubators for deep microbial life. *Proc. Natl. Acad. Sci.* **114**, 4324–4329.

Rinaudo C., Gastaldi D. and Belluso E. (2003) Characterization of chrysotile, antigorite and lizardite by FT-Raman spectroscopy. *Can. Mineral.* **41**, 883–890.

Rouméjon S., Andreani M. and Früh-Green G. L. (2019) Antigorite crystallization during oceanic retrograde serpentinization of abyssal peridotites. *Contrib. Mineral. Petrol.* **174**, 60.

Sachan H. K., Mukherjee B. K. and Bodnar R. J. (2007) Preservation of methane generated during serpentinization of upper mantle rocks: Evidence from fluid inclusions in the Nidar ophiolite, Indus Suture Zone, Ladakh (India). *Earth Planet. Sci. Lett.* **257**(1–2), 47–59.

Scambelluri M., Hoogerduijn-Strating E. H., Piccardo G. B., Vissers R. L. M. and Rampone E. (1991) Alpine olivine- and titanian clinohumite-bearing assemblages in the Erro-Tobbio peridotite (Voltri Massif, NW Italy). *J. Metamorph. Geol.* **9**, 79–91.

Scambelluri M., Fiebig J., Malaspina N., Müntener O. and Pettke T. (2004) Serpentinite subduction: implications for fluid processes and trace-element recycling. *Int. Geol. Rev.* **46**(7), 595–613.

Schrenk M. O., Brazelton W. J. and Lang S. Q. (2013) Serpentinization, carbon, and deep life. *Rev. Mineral. Geochem.* **75**, 575–606.

Seitz J. C., Pasteris J. D. and Chou I.-M. (1993) Raman spectroscopic characterization of gas mixtures; I, Quantitative composition and pressure determination of CH_4, N_2 and their mixtures. *Am. J. Sci.* **293**, 297–321.

Song S., Su L., Niu Y., Lai Y. and Zhang L. (2009) CH_4 inclusions in orogenic harzburgite: Evidence for reduced slab fluids and implication for redox melting in mantle wedge. *Geochim. Cosmochim. Acta* **73**(6), 1737–1754.

Song S., Niu Y., Su L. and Xia X. (2013) Tectonics of the North Qilian orogen, NW China. *Gondwana Res.* **23**(4), 1378–1401.

Vacquand C., Deville E., Beaumont V., Guyot F., Sissmann O., Pillot D., Arcilla C. and Prinzhofer A. (2018) Reduced gas seepages in ophiolitic complexes: Evidences for multiple origins of the H_2-CH_4-N_2 gas mixtures. *Geochim. Cosmochim. Acta* **223**, 437–461.

Vitale Brovarone A., Martinez I., Elmaleh A., Compagnoni R., Chaduteau C., Ferraris C. and Esteve I. (2017) Massive production of abiotic methane during subduction evidenced in metamorphosed ophicarbonates from the Italian Alps. *Nat. Commun.* **8**, 14134.

Wang D. T., Reeves E. P., McDermott J. M., Seewald J. S. and Ono S. (2018) Clumped isotopologue constraints on the origin of methane at seafloor hot springs. *Geochim. Cosmochim. Acta* **223**, 141–158.

Whitney D. L. and Evans B. W. (2010) Abbreviations for names of rock-forming minerals. *Am. Mineral.* **95**(1), 185–187.

Wunder B. and Schreyer W. (1997) Antigorite: High pressure stability in the system MgO-SiO_2-H_2O (MSH). *Lithos* **41**, 213–227.

Zhang L., Sun W.-D., Zhang Z., An Y. and Liu F. (2019a) Iron isotopic composition of supra-subduction zone ophiolitic peridotite from northern Tibet. *Geochim. Cosmochim. Acta* **258**, 274–289.

Zhang L., Sun W.-D. and Chen R.-X. (2019b) Evolution of serpentinite from seafloor hydration to subduction zone metamorphism: Petrology and geochemistry of serpentinite from the ultrahigh pressure North Qaidam orogen in northern Tibet. *Lithos* **346-347**, 105158.

Associate editor: Frieder Klein